Heliyon 9 (2023) e19744

Contents lists available at ScienceDirect

Heliyon

journal homepage: www.cell.com/heliyon

Indium-zinc-oxide thin films produced by low-cost chemical solution deposition: Tuning the microstructure, optical and electrical properties with the processing conditions

Izabela Stojanoska [a], Miha Okorn [a], Brigita Kmet [a], Hana Uršič [a], Vera Gradišnik [b,d], Duško Čakara [c,d], Janez Kovač [a], Danjela Kuscer [a,*]

[a] Jožef Stefan Institute, Ljubljana, Slovenia
[b] University of Rijeka, Faculty of Engineering, Rijeka, Croatia
[c] University of Rijeka, Department of Biotechnology, Croatia
[d] Center for Micro- and Nanosciences and Technologies, Rijeka, Croatia

ARTICLE INFO

Keywords:
Chemical solution deposition
Indium zinc oxide
Thin films
Microstructure

ABSTRACT

Indium-zinc-oxide (IZO) films were prepared by spin coating an ethanol-ethylene-glycol precursor solution with a Zn/(In + Zn) ratio of 0.36 on glass. The effects of temperature on the structure, microstructure, electrical, and optical properties of the IZO thin films were investigated by thermal analysis, Fourier-transform infrared spectroscopy, X-ray diffraction, electron and atomic-force microscopy, X-ray photoelectron spectroscopy and variable-angle spectroscopic ellipsometry. The prepared IZO thin films heated at 500, 600, and 700 °C in air were transparent, without long-range ordering, and with an RMS surface roughness of less than 1 nm. The lowest electrical resistivity at room temperature, 0.0069 Ωcm, was observed for the 115-nm-thick IZO thin film heated at 600 °C in air and subsequently post-annealed in Ar/H_2. The thin film exhibited a microstructure characterized by grains typically 20 nm in size and had no organic residues. This film exhibits uniaxial optical anisotropy due to its ultra-thin lamellae with a high electron density. The ordinary refractive index was fitted as a Tauc-Lorentz-Urbach function, which is typical of an indirect absorption edge occurring in amorphous semiconductor materials. The principal absorption peak with an onset at about 2.8 eV and a Tauc gap energy of ~2.6 eV is similar to those observed for In_2O_3. The described process of chemical solution deposition and subsequent curing is promising for the low-cost fabrication of IZO thin films for transparent electronics, and can be used to tune the structure and microstructure of IZO thin films, as well as their electrical and optical properties.

1. Introduction

Transparent electronics is a rapidly developing area of science and technology focusing on the manufacture of invisible electronic circuits and devices, the functions of which are based on a transparent, conductive material (TCM). Next-generation device technology requires TCM layers on transparent substrates such as glass with thicknesses up to a few hundred nanometers and a high optical transmittance (>90%), while the electrical sheet resistance (R_s) requirements are application-specific and range from 1 to 500 Ω/sq

* Corresponding author.
E-mail address: danjela.kuscer@ijs.si (D. Kuscer).

https://doi.org/10.1016/j.heliyon.2023.e19744
Received 10 March 2023; Received in revised form 30 August 2023; Accepted 31 August 2023
Available online 1 September 2023

[1–3]. The most commonly used composition for transparent conductive materials (TCM) is indium tin oxide (ITO), which is characterized by a thickness of less than 1 μm, a sheet resistance of about 10 Ω/sq, and an optical transmittance of more than 80%. Physical-vapor- deposition methods such as magnetron sputtering followed by post-deposition curing above 400 °C are well established for the commercial production of ITO thin films. However, expensive materials and vacuum-based deposition methods are forcing researchers to search for more economical materials and processes [4,5].

Among the metal oxides, In–Zn–O (IZO) thin films with a Zn/(In + Zn) ratio between ~0.15 and ~0.45 have attracted much attention due to their tendency to be amorphous with very smooth surfaces after sputtering and heating to 600 °C. Amorphous compositions have an electrical conductivity of ~1 mΩcm and an optically transparency over 80%, a wide bandgap of ~3.6 eV and a high etching rate, which is required for the micropatterning process. These properties ensure easy device integration at low processing temperatures and the production of devices with uniform properties [2,3,6–11].

A systematic study of the electrical properties of IZO thin films was performed on magnetron-sputtered samples using Van der Pauw and Hall measurements. The IZO thin films were found to be n-type semiconductors with oxygen vacancies ($\ddot{V}_o$), interstitial Zn ($\ddot{Z}n_i$), and indium on zinc (In_{zn}·) as the source of donors. The type and amount of defects and their mobility in the thin films are influenced not only by the chemical composition, but also by factors such as the deposition conditions, post-deposition curing, crystal structure, thickness, and microstructure of the film [9,12–15]. For example, Tsai et al. [12] suggested that the high resistivity of amorphous IZO thin films with very low thicknesses could be related to the large strain and defect homogenization in the layer. These effects become less important for film thicknesses above 100 nm. Existing literature also shows that after-annealing of IZO thin films in an atmosphere containing hydrogen leads to an increase in their electrical conductivity. Hydrogen located in the interstitial positions in the ZnO structure serves as a shallow donor and thus increases the number of free charge carriers [16]. However, a discussion related to an IZO thin film's microstructure and its influence on electrical conductivity is not well documented.

Optical studies of mixed transition-metal oxide films are routinely implemented with UV/VIS/NIR transmission spectrophotometry, which was also reported for IZO films prepared by different routes [11,17,18]. The transparency in the VIS range was found to depend on both the In:Zn ratio and the crystallinity. For crystalline IZO, the transmittance was found to increase with an increasing content of In, reaching values of >95% for the $In_{0.06}Zn_{0.94}O$ stoichiometry [17]. For amorphous IZO films with a In:Zn ratio of 5.5:1, prepared by magnetron sputtering without post-deposition heating, the transmittance is <90% [18]. For the films with a In:Zn ratio of 7:3 prepared by spin coating, the transmittance of 82–85% was found not to depend so much on the annealing temperature, but rather to decrease slightly with the number of deposition layers [11]. A direct band gap is proposed in the description of the magnetron-sputtered films, irrespective of the crystallinity, while the band-gap energy was found to be very similar to ZnO (3.25 eV) for Zn-rich IZO films, and slightly higher (around 3.45 eV) for In-rich IZO films [17,18]. Nevertheless, the relationships between the transmittance and electrical conductivity as macroscopically observable properties, on the one hand, and the internal film structure, its optical symmetry, the parameters of the dielectric function such as the band-gap energy and nature, on the hand, are not yet clarified for these films.

IZO thin films have been prepared by numerous techniques, including magnetron sputtering, pulsed-laser deposition, chemical vapor deposition, and chemical solution deposition [12,19–23]. In comparison, spin coating is a low-cost, simple, vacuum-free technique for processing thin films under normal conditions (1 bar, room temperature). It allows thickness control using a layer-by-layer approach, control of the chemical composition and a homogeneous distribution of dopants in the main phase, which is especially important for multicomponent thin films to tailor their functional properties. The microstructure of the thin films is adjusted by post-deposition curing, in particular by annealing at temperatures of several hundred °C to remove organic compounds and induce the formation of metal oxides [24].

The transparent, stable solutions are usually prepared from zinc acetate (ZA) and indium nitrate (IN) dissolved in 2-methoxyethanol with the addition of stabilizers such as ethanolamine, acetylacetone, and acetic acid [13,22,25,26]. It was previously shown that upon heating the solution, the ZA and IN decompose and hydrolyze to form M − OH up to 130 °C, followed by the dehydration of M − OH that occurs up to 250 °C and crystallization of the oxide between 300 and 400 °C [27,28]. Spin-coating-derived IZO thin films have mostly been processed at temperatures above 500 °C to effectively remove the organic additives and induce densification. However, such temperatures crystalize the ZnO. For example, upon heating IZO layers with Zn/(In + Zn) ratios between 0.2 and 0.8 to 650 °C, all these films crystallized, although they had an optical transparency over 80% and a sheet resistance in the range of mΩcm [7]. Ullah et al. [11] also reported on polycrystalline IZO thin films processed by spin coating at 500 and 600 °C. They demonstrated that a higher processing temperature improves the charge-carrier mobility, while the film's porosity has the opposite effect. The ~300-nm-thick films possessed high transparency, while the highest electrical conductivity of 7.66 mΩcm was obtained for the In-rich thin film processed at 600 °C. On the other hand, the 185-nm-thick IZO thin films with a Zn/(In + Zn) ratio of 0.2, which were spin coated on a silicon substrate and then heated at 450 °C in air, exhibited an amorphous, organic-free structure and grains ranging in size from 20 to 50 nm. Unfortunately, the electrical and optical properties of these films have not been reported [26]. While there have been studies on IZO thin films produced through chemical solution deposition, the majority of existing reports concentrate either on the preparation and characterization of the material [26], or an electro-optical analysis [9,10,29]. A direct comparison between the microstructural and functional properties of IZO thin films is therefore extremely difficult or even impossible, although it would improve our understanding of the relationship between processing and properties and thus the effective design of their functional properties.

The objective of this study was to process IZO thin films with identical nominal chemical compositions from solutions by low-cost spin coating and to investigate the effects of different processing temperatures (500 °C, 600 °C and 700 °C) on their thickness, surface roughness, structure, microstructures and sheet resistance. Of particular interest was the 110-nm-thick amorphous IZO thin film processed at 600 °C in air, which exhibited the lowest sheet resistance among the IZO thin films annealed in air. This sample was post

annealed in Ar/H_2 to understand how post annealing at 500 °C affects the thickness, microstructure, crystallinity, surface roughness and sheet resistance. A direct comparison of the two IZO thin films showed that the post annealing affects the electrical conductivity of the thin film, but has little effect on its structure and microstructure. We also showed that the use of spectroscopic ellipsometry in the visible and NIR ranges for the optical characterization of such films, in addition to the standard information on absorption and transmittance, provides important information on the complex dielectric function and nanoscale structuring of films prepared by chemical solution deposition. This study provides valuable insights into optimizing the chemical solution deposition process and the development of transparent, conductive IZO thin films for next-generation electronic devices.

2. Experimental

2.1. Solutions

The solutions were formulated using zinc acetate dihydrate (ZAH, >99%, $Zn(CH_3COO)_2$. X H_2O, Sigma Aldrich, St. Louis, MO, USA), indium nitrate hydrate (INH, $In(NO_3)_3$. xH_2O, 99.9%, Alfa Aesar, Karlsruhe, Germany), anhydrous ethanol (C_2H_5OH, 99.9%, Carlo Erba, Val-de-Reuil, France), ethylene glycol ($C_2H_6O_2$, EG 99.5%, Riedel-de Haën, Seelze, Germany) and acetic acid (CH_3COOH, 100%, Alfa Aesar, Karlsruhe, Germany).

The spin coating solution was created by combining a Zn solution and an In solution in a 1:1 volume ratio, which corresponded to a nominal film composition of 75 wt % of In_2O_3 and 25 wt % of ZnO, or to the molar ratio x = Zn/(In + Zn) of 0.36 (IZO).

A zinc solution with concentrations of Zn 0.106 mol L^{-1} was prepared by dissolving ZAH in ethylene glycol utilizing a flask equipped with a magnetic stirrer, and allowing the mixture to stir at room temperature for 1 h. An indium solution with a concentration of 0.187 mol L^{-1} was prepared by dissolving the INH in anhydrous ethanol with the addition of 0.425 vol % acetic acid. The INH was weighed in a dry box and mixed with ethanol. The mixture was agitated in a flask with a magnetic stirrer under a dry nitrogen atmosphere at room temperature for 10 min, followed by stirring in ambient air at 40 °C for 20 min. The mixture was cooled naturally to room temperature. The acetic acid was added dropwise to the solution and stirred for 1 h. The IZO solution with a concentration of 0.147 mol L^{-1} was prepared by mixing the zinc solution and the indium solution in a volume ratio of 1:1. All the solutions were transparent, free of particles, and remained stable for over a month when stored in a refrigerator.

Thermal decomposition of the solution was investigated through techniques thermogravimetry (TG), differential thermal analysis (DTA), and evolved-gas analysis (EGA). These analyses were conducted using a simultaneous thermal analyzer connected to a mass spectrometer (STA 409, Netzsch, Selb, Germany, and ThermoStar, Balzers Instruments, Oerlikon, Switzerland). Before the analysis, the IZO solution underwent a drying process in air at 200 °C for a duration of 20 h. Approximately 25 mg of the resulting powder was positioned in a Pt crucible and subjected to heating, gradually raising the temperature from ambient conditions to 600 °C. This heating process occurred within a controlled flow of synthetic air (100 mL min^{-1}), at a heating rate of 10 K/min.

2.2. Thin films by spin coating

The IZO precursor solution was applied onto soda-lime glass (with dimensions of 12 mm × 12 mm and a square shape, sourced from Corning Eagle XG) using a spin coating technique at a speed of 3000 revolutions per minute for a duration of 30 s (equipment: Headway research). The coated samples were then subjected to heating on a hot-plate, first at 200 °C for 2 min, followed by 350 °C for 2 min. This procedure was iterated ten times. Afterward, the prepared samples underwent annealing in an air environment at temperatures of 500 °C, 600 °C, and 700 °C, each for a period of 15 min. These samples were designated as IZO5, IZO6, and IZO7, respectively. For sample IZO6, an additional treatment involved heating it at 500 °C for 60 min under an Ar/H_2 atmosphere, resulting in IZO6-Ar/H_2.

The IZO precursor solution was deposited on soda-lime glass (square shape with dimensions 12 mm × 12 mm, Corning Eagle XG) using a spin coating at 3000 min^{-1} for 30 s (Headway research). The coated samples were then subjected to heating on a hot-plate, first at 200 °C for 2 min, followed by 350 °C for 2 min. The procedure was repeated ten times, after which the samples were annealed in air at 500, 600, and 700 °C for 15 min. The samples are denoted as IZO5, IZO6 and IZO7, respectively. Sample IZO6 was additionally heated at 500 °C for 60 min in Ar/H_2 (IZO6-Ar/H_2).

2.3. Structural and microstructural characterization of the thin films

The investigation of the thin films involved the utilization of grazing-incidence (GI) X-ray diffraction (XRD) using a Malvern PANalytical Empyrean diffractometer (Almelo, The Netherlands) with Cu-Kα1 radiation (λ = 1.5406 Å) at 45 kV and 40 mA. An incident-beam side hybrid monochromator with a 1/16° slit was employed, while the diffracted-beam side employed a parallel-plate collimator. The fixed GI angle (ω) was maintained at 1°. The diffractograms were collected in the 2θ range from 20° to 60° with a step size of 0.02° and a counting time of 20 s.

Both the surface and the cross-section of the thin films were examined using a field-emission scanning electron microscope (FE-SEM) Verios 4G HP (Thermo Fischer, Waltham, Massachusetts, USA). Before undergoing analysis, a 1-nm-thick layer of Au/Pd was applied to the films using PECS 682 (produced by Gatan, Pleasanton, CA, USA). The surface of the thin films was investigated with an atomic force microscope (AFM, MFP-3D, Asylum Research Molecular Force Probe 3D, MFP-3D, Santa Barbara, CA, USA) in AC topography mode. Tetragonal silicon probes (OMCL-AC160 TS-R3, Olympus, Japan) were used for the scanning. The 1.5 μm × 1.5 μm areas were scanned and the surface roughness (root-mean-square roughness, RMS) was calculated.

The IZO5, IZO6 and IZO7 thin films, and the ZnO and In_2O_3 powders were analyzed by Fourier-transform infrared spectroscopy

(FTIR) using a Perkin Elemer Spectrum 100. The transmittance data were collected in the range 380–4000 cm^{-1} in the attenuated total reflectance (ATR) mode using a diamond crystal with a refractive index of 2.4.

The X-ray photoelectron spectroscopy (XPS) analyses were carried out on PHI-TFA XPS spectrometer (Physical Electronics Inc.) equipped with an Al-monochromatic source. The surface composition was quantified from the XPS peaks Zn $2p_{3/2}$, In $3d_{5/2}$ and O 1s, considering the relative sensitivity factors provided by the instrument manufacturer [30]. Before the XPS analyses the surface of the sample was sputtered with an Ar-ion beam of energy 1 keV for 10 min to remove the surface contamination. In this way we removed a surface layer with a thickness of about 10 nm.

2.4. Electrical resistivity of the thin films

The sheet resistance (R_s) of the thin films was determined using the four-point probe technique [31], where the probes were systematically positioned equidistantly along a line. The measured voltage drop (V) between the two inner probes and the current (I) through the outer probe were used to calculate the R_s. The following equation was used for this calculation:

$$R_s = \mathrm{C}\,\frac{\pi}{\ln(2)}\,\frac{\Delta V}{I}$$

where C is a correction factor. For square-shaped samples with dimensions of 12 mm × 12 mm and a spacing s of 1.5 mm, $C = 0.88$. The resistivity of the film is obtained by multiplying the R_s by the film thickness.

2.5. Variable-angle spectroscopic ellipsometry

The ellipsometric spectra were measured for the sample IZO6 in the wavelength (λ) range 360–1200 nm, at three different angles of incidence (AOI). The variable step in λ was adjusted such that 30 data points are measured within the range, with a constant difference in the EM radiation energy ($\Delta E \approx 0.069$ eV) between the measurements. The nulling method was applied to obtain the ellipsometric angles [Ψ,Δ] from the measured signal as an average of the measurements performed in four zones. A beam cutter was used to eliminate the reflection from the bottom surface of the glass substrate. The measurements were performed with an EP4 imaging ellipsometer from Accurion (Göttingen, Germany).

For the surface of a semi-infinite glass slide, $\tilde{n}(\lambda)$ the "effective substrate" complex refractive-index dispersion, ($\tilde{n}(\lambda) = n(\lambda) + i \bullet k(\lambda)$), was obtained via a mathematical inversion of [Ψ,Δ] measured for the substrate in the absence of the studied film [32]. The resulting $\tilde{n}(\lambda)$ matches the Cauchy function typically measured for Corning glass. The dispersion of the film was fitted from the experimental ellipsometric spectra by implementing an optical model that invokes the Fresnel formulae for calculating the (p-, s-) amplitude reflectivity coefficients for a stack of optically stratified materials (see inset in Fig. 8) [32]. The best fit was achieved by implementing a uniaxially anisotropic dispersion for the IZO6 film, in which the ordinary component is represented by the

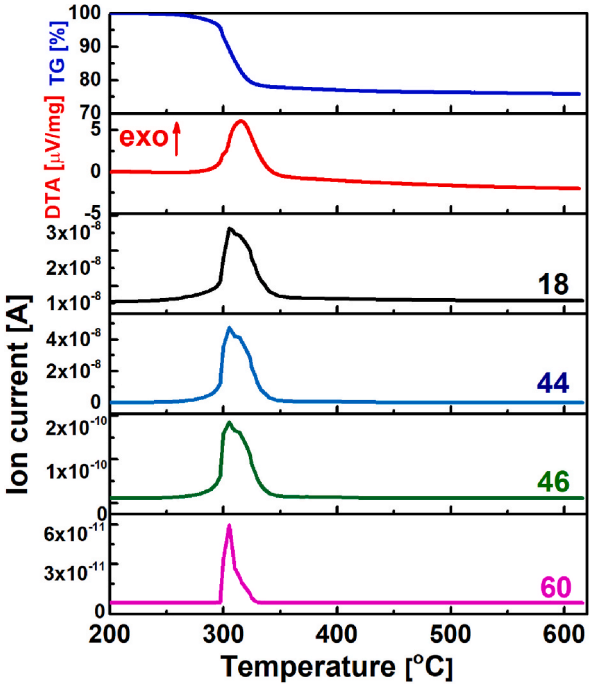

Fig. 1. TG/DTA/EGA curves of precursor solution dried at 200 °C. 18-water, 44-CO_2, 46-NO_x and 60-CH_3COOH.

Tauc-Lorentz-Urbach (TLU) oscillator [33], and the extraordinary component by a purely real *n*. To improve the reliability of the optical model and the fitted dispersion, the film thickness was fixed to the value observed from the SEM. In this way, only insignificant correlations were found among the eight fitted parameters, and thus there was no overfitting; however, some of the parameters, which point to an absence of overfitting, were obtained with relatively large confidence intervals. All attempts to fit the experimental ellipsometric spectra by implementing an isotropic dispersion for the film, or one that does not imply an Urbach tail, resulted in significantly poorer fits, and were thus discarded as an option.

3. Results

3.1. Structure and microstructure of IZO thin films

Fig. 1 shows the TG-DTA-EGA curves for a precursor solution dried at 200 °C. The TG curve showed a weight loss of 20.65% from 200 to 325 °C. Upon further heating to 600 °C the sample gradually lost 3.25% of its weight. The weight loss up to ~350 °C was accompanied by the evolution of water, NO_x, CO_2 and acetic acid, suggesting the decomposition and oxidation of the organic components. These processes are also reflected in the DTA curve, which shows a broad exothermic peak between 300 and 350 °C. This peak contains at least two overlapping peaks, one associated with the decomposition and oxidation of the organic residues and the other with the formation of metal oxide crystallites. A similar decomposition and phase transformation was observed for ZnO thin films derived from the sol-gel process [34]. The observed TG/DTA profiles are consistent with expectations, as the temperature of the amorphous-crystalline transition for In_2O_3 and ZnO is reported to be above 250 °C and 300 °C, respectively [35–37].

Taking into account the outcomes of the thermal analysis of the dried IZO precursor solution, we selected the annealing conditions for processing the IZO thin films. These parameters entailed an initial drying step at 200 °C and 350 °C for 2 min, followed by annealing at temperatures of 500 °C (IZO5), 600 °C (IZO6), and 700 °C (IZO7) for 15 min in air. The thin film with the lowest sheet resistance, IZO6 (see Section 3.2) was additionally annealed at 500 °C for 1 h in Ar/H_2 (IZO6-Ar/H_2).

To complement the thermal analyses, particularly to determine the presence of organic residues, we performed FTIR spectroscopy on IZO5, IZO6, IZO7 and IZO6-Ar/H_2 (Fig. 2a). The observed infrared spectra of all the samples are similar, while the FTIR spectrum of the glass is shown for comparison. The absorption peaks at 1370, 1020, 915, 780 and 670 cm^{-1} were detected for all the samples and are characterized for an alkaline-earth borosilicate glass, i.e., the substrate. The absorption peaks at 1370 cm^{-1} and 670 cm^{-1} are attributed to the stretching and bending vibrations of the B–O bond, respectively. The peak at 1020 cm^{-1} belongs to the antisymmetric stretching vibration of the B–O bond and the bending vibration of the Si–*O*–Si bond. The peak at 915 cm^{-1} is associated with the B–O and Si–*O*–B bonds, while the peak at 780 cm^{-1} is assigned to the stretching vibration of O–Si–O [38]. The characteristic bands of the glass, observed in the FTIR spectra of the thin films, suggest that part of the light travels into the glass substrate. This is not surprising since the penetration depth of the evanescent wave into the IZO ranges from ~1 to ~10 μm, which is much thicker than the IZO thin films, ~100 nm (see supplementary, S1). Any characteristic bands of the nitro and aceto groups in the range 1450–1340 cm^{-1}, which could originate from the precursor solution, were not observed, confirming the disappearance of these bands upon heating the sample to 500 °C. However, a broad band between 3200 and 3600 cm^{-1} was observed in IZO5, which could be assigned to the stretching vibrations of the O–H bond, indicating the presence of M − OH residues in the thin film annealed at 500 °C. This adsorption peak is negligible in IZO6 and disappeared in IZO7. Only for IZO7 were three absorption peaks detected in the region below at 600 cm^{-1}, i.e., at 600, 560, and 536 cm^{-1} (see inset in Fig. 2a). These bands were also observed for the In_2O_3 powder, which was measured as a reference (Fig. 2b). The characteristic band for ZnO at ~670 cm^{-1}, which can be seen in the spectrum of the ZnO powder, is located at the same position as that for the glass substrate [39].

The XRD patterns of IZO5, IZO6, IZO7 and IZO6-Ar/H_2 are similar and characterized by a high background and two broad diffraction peaks (Fig. 3). The diffraction peak at 2 theta equals ~22° with a low intensity corresponds to the peak identified for the

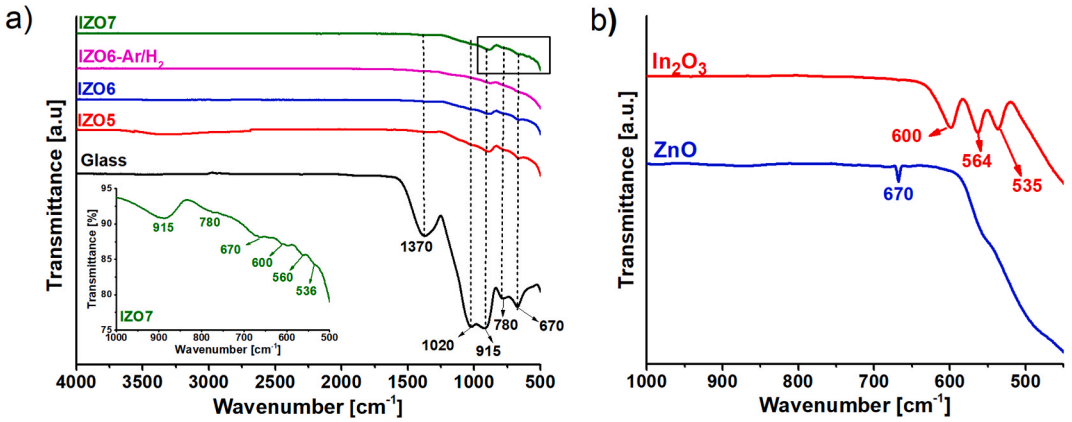

Fig. 2. a) FTIR spectra of IZO5, IZO6, IZO6-Ar/H_2 and IZO7. The spectrum of the glass substrate is added as a reference. b) FTIR spectra of In_2O_3 powder and ZnO powder.

glass substrate. The broad diffraction peak, also of low intensity, between 30° and 35° indicates that the structures of all the IZO thin films lack the long-range order. The diffraction peak could be related to the cubic bixbyite structure of In_2O_3 (PDF 04-010-3287), to hexagonal ZnO (04-004-4531), and/or to homologous $In_2O_3(ZnO)_k$ compounds, for example $In_2O_3(ZnO)_3$ (PDF 01-077-8495).

The bixbyite structure of In_2O_3 exhibits diffraction peaks with 100% and 30% intensity at 30.5° and 35.5°, respectively. The hexagonal structure of ZnO exhibits diffraction peaks at 31.7° (intensity 55%), 34.4° (intensity 41%), and 36.2° (intensity 100%), with the most intense peak barely visible in the spectra. The rhombohedral structure of $In_2O_3(ZnO)_3$ shows diffraction peaks with 100% and 95% intensity at 34.1° and 35.2°, respectively, and four diffraction peaks between 30.8° and 32°. Although the formation of $In_2O_3(ZnO)_k$ was confirmed at a temperature of >1000 °C in the In_2O_3–ZnO system [40], the $In_2O_3(ZnO)_k$ phases were observed in IZO thin films processed at much lower temperatures, ≤550 °C [19,41]. We assume that the IZO thin films consist of a mixture of two crystalline phases, i.e., cubic In_2O_3 and rhombohedral $Zn_kIn_2O_{3+k}$, in agreement with the literature [28,41].

A representative fracture cross-section and surface SEM images of the IZO5, IZO6, IZO6-Ar/H_2 and IZO7 films are shown in Figs. 4 and 5, respectively. The thickness of IZO5 is 130 nm, while a thickness of about 115 nm was estimated for IZO6, IZO6-Ar/H_2 and IZO7. Careful examination of the SEM cross-sectional images revealed that IZO6 consisted of ten distinct layers. In IZO5 the layered structure was less clear, while in IZO7 no distinct layers could be identified. The layered structure should be attributed to the successive deposition of ten layers, each heated to 200 °C and 350 °C. Heating the deposition solution to 200 °C leads to the evaporation of the solvents, ethanol and ethylene glycol, with boiling points of 78 °C and 197 °C, respectively. Most of the organic components decompose when heated below 350 °C, followed by the formation of crystallites, which is evident from the exothermic peak in this temperature range (Fig. 1) [42]. SEM and AFM images of the air-annealed samples (Fig. 4 a-c, Fig. 5 a-c, Fig. 6 a-c) show that IZO5 has a smooth surface and a RMS surface roughness of 200 p.m. The observed film morphology is granular, with a grain size in the range of a few nanometers. When the temperature was increased to 600 °C, the grains grew to a size of ~20 nm within a single layer. The sample IZO6 had a uniform and smooth surface with an RMS surface roughness of 480 p.m. (Fig. 4 b, Fig. 5 b, Fig. 6 b). When the temperature was further increased to 700 °C, the grains continued to grow and the individual layers disappeared. The SEM micrograph for IZO7 shows the largest RMS surface roughness of 970 p.m. and the formation of larger grains (G) within the matrix phase (M) (Fig. 4 c,Fig. 5 c, Fig. 6 c), which should originate from the mixture of two phases in thin films, i.e., In_2O_3 and $In_2O_3(ZnO)_3$ [11,40]. For IZO6-Ar/H_2 the thickness, microstructure and grain size were similar to IZO6. It had a uniform and smooth surface with nanosized grains and an RMS surface roughness of 500 p.m. (Fig. 5 d, Fig. 6 d). It should be noted that the distinct layers were less noticeable for IZO6-Ar/H_2 (Fig. 4 d) which derives from the fact that this sample was additionally annealed at 500 °C for 1 h. This slightly increases the grain size. However, it is worth mentioning here that annealing the IZO6 thin film in Ar/H_2 does not critically influence the structure, grain size, thickness and microstructure of IZO6-Ar/H_2 thin films.

To further elucidate the properties of the IZO thin films we analyzed the IZO6 and IZO6-Ar/H_2 by XPS. We analyzed the surfaces of the as-prepared thin films, and the surfaces of the thin films etched for 10 min, which corresponds to a thin film at a depth of approximately 10 nm from the surface. We detected some carbon originating from contamination at the as-prepared surface of both IZO thin films, while it was not detected in the etched films at a depth of 10 nm. This suggests that the carbon originates from the environment. Fig. 7 shows the XPS spectra measured at a depth of 10 nm for IZO6 and IZO6-Ar/H_2. The elements indium, zinc and oxygen were detected. No other elements were detected in the XPS spectra, suggesting that the diffusivity of elements from the glass substrate to the IZO thin film, e.g., Si, is unlikely to occur. The chemical compositions in at. % obtained from the XPS spectra Zn $2p_{3/2}$, In $3d_{5/2}$ and O 1s are given in Table 1. The Zn/(In + Zn) ratio of both IZO thin films agreed well with the nominal chemical composition of the solution with a Zn/(In + Zn) ratio of 0.36. Hence, these data show that the chemical composition of the IZO thin films is similar to the nominal composition after firing the IZO thin film at 600 °C for 15 min in air as well as after additional annealing of this sample at 500 °C for 60 min in Ar/H_2.

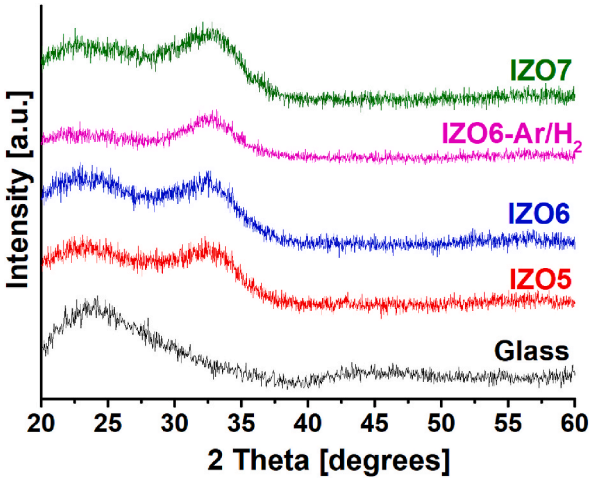

Fig. 3. XRD spectra of IZO5, IZO6, IZO7, IZO6-Ar/H_2 and glass.

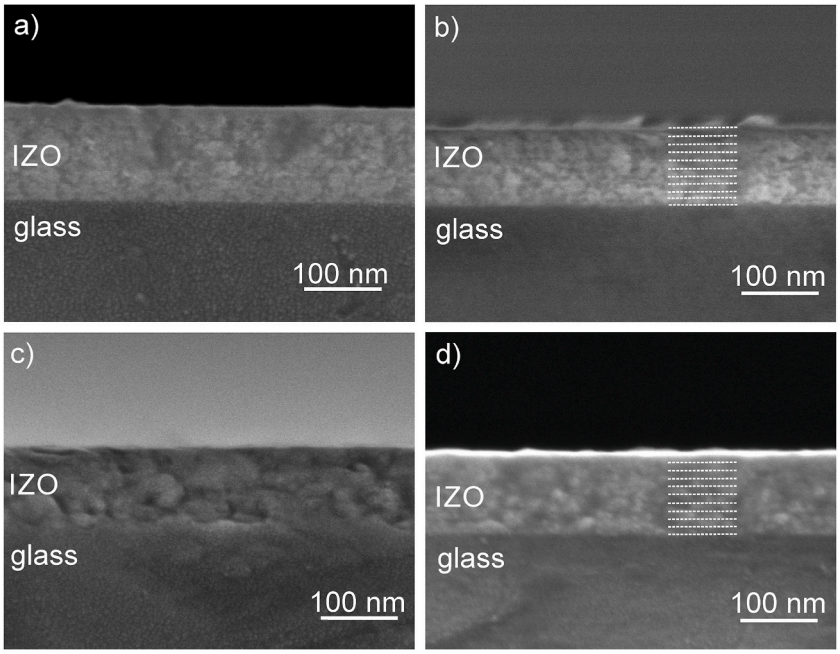

Fig. 4. SEM cross-section of thin films a) IZO5, b) IZO6, c) IZO7 and d) IZO6-Ar/H_2.

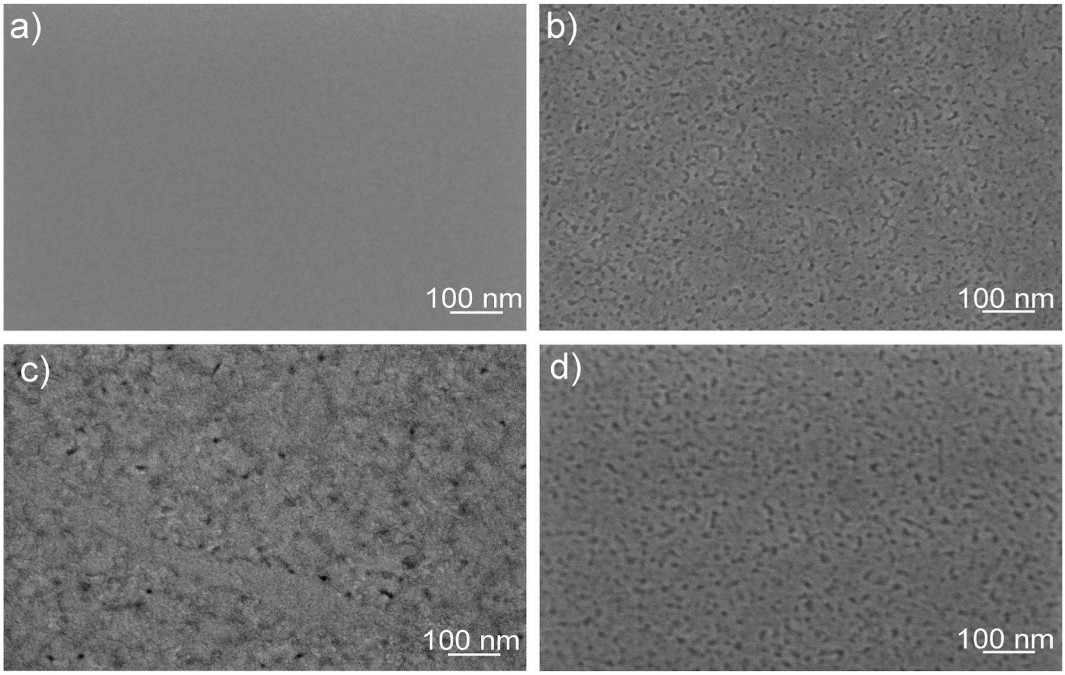

Fig. 5. SEM surface images of thin films a) IZO5, b) IZO6, c) IZO7 and d) IZO6-Ar/H_2.

3.2. Electrical properties of IZO thin films

The sheet resistance R_s of IZO5, IZO6, and IZO7 was the highest immediately after annealing in air and decreased with time, which could be due to their interactions with the atmosphere. A similar phenomenon was observed for pure ZnO and Ga-modified ZnO [11, 43]. The R_s becomes constant about two weeks after the sample preparation. The R_s values of the samples measured two weeks after their preparation are listed in Table 2.

The R_s of the IZO thin films decreases with increasing processing temperature from 500 to 600 °C, while IZO7 had the largest R_s.

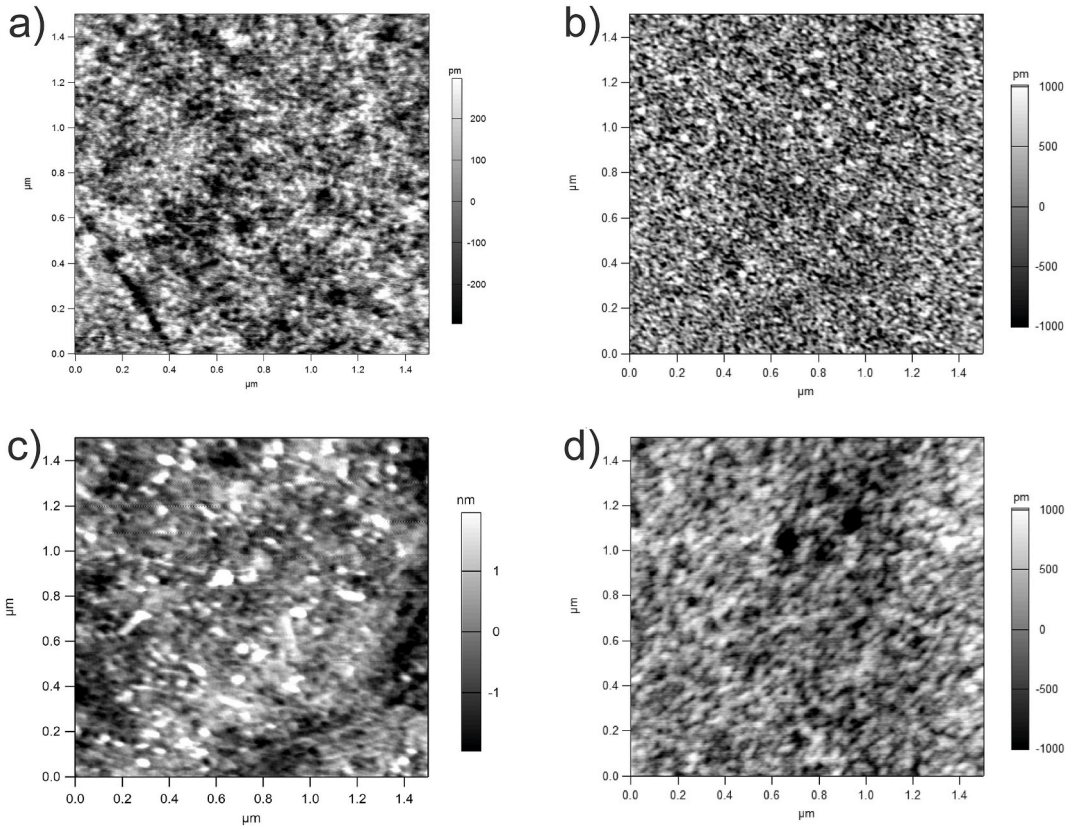

Fig. 6. AFM image of the thin films a) IZO5, b) IZO6, c) IZO7 and d) IZO6-Ar/H_2.

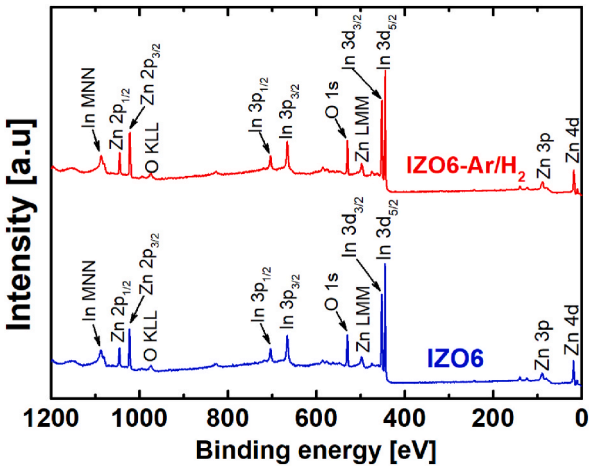

Fig. 7. XPS survey spectra of the IZO6 and IZO6-Ar/H_2 at the depth of 10 nm.

The R_s of the samples depends on the carrier concentration and mobility. For IZO thin films, the charge carriers, i.e., the conduction electrons, originate from the oxygen vacancies and from the substitutional and/or interstitial metal ions, while their mobility depends on the microstructure of the thin films [20,41].

IZO5 and IZO6 did not exhibit long-range ordering and are composed of nanoscale grains. The IZO5 contained M − OH residues, as shown by the FTIR spectroscopy, which contribute to greater resistivity. On one hand, the IZO6 was thinner, and had a negligible amount of residue, which effectively improves the carrier mobility and thus increases the electrical conductivity. On the other hand, the distinct layers observed in IZO6 might cause the electron scattering, which contributes to a lower carrier mobility. Interestingly, the R_s value of IZO7, for which the distinct layers were not observed, is an order of magnitude larger than that of IZO6, although its

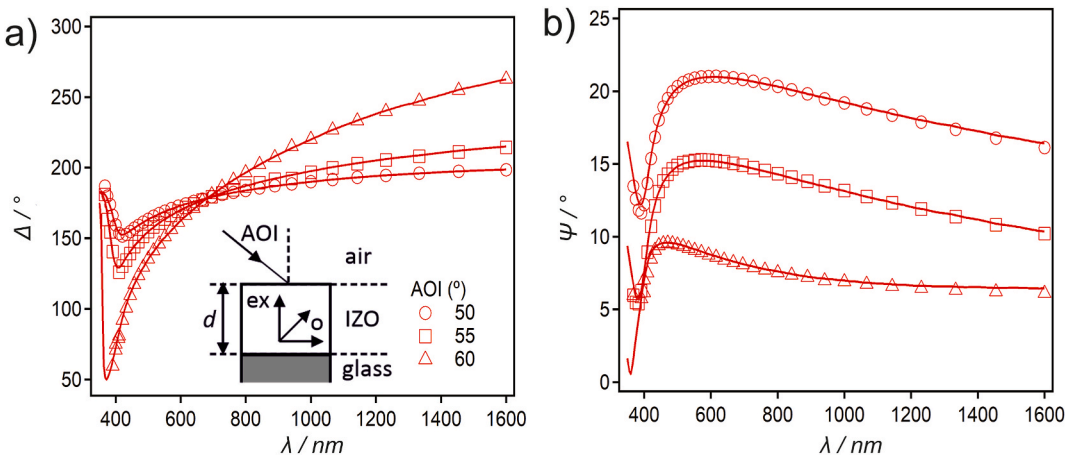

Fig. 8. The best-fit ellipsometric spectra (solid lines) obtained from fitting the optical model (inset), versus the experimental data measured for IZO6 at three AOIs (symbols, see legend). Figures a) and b) display the ellipsometric angles Δ and Ψ, respectively.

Table 1
Nominal chemical composition and chemical composition obtained from the XPS spectra at a depth of 10 nm for IZO6 and IZO6-Ar/H_2.

	Nominal composition [at %]	IZO 6 [at %]	IZO6-Ar/H_2 [at %]
O	56.8	49.3	49.0
In	27.5	31.8	31.9
Zn	15.8	18.9	19.1
Zn/(In + Zn)	0.36	0.373	0.375
In:Zn	1.76:1	1.68:1	1.67:1

Table 2
Thickness, sheet resistance R_s and electrical resistivity ρ of IZO5, IZO6 IZO7 and IZO6-Ar/H_2 thin films.

Sample	Thickness [nm]	R_s [kΩ/sq]	ρ [Ohm cm]
IZO5	130	220 ± 2	2.8
IZO6	115	40 ± 1	0.45
IZO7	115	1129 ± 9	12.6
IZO6-Ar/H_2	115	0.600 ± 0.01	0.0069

thickness is similar to that of IZO6. We attribute this observation to the fact that IZO7 contains larger grains that perturb the matrix phase and contribute to a lower carrier mobility, which is consistent with Steigert et al. [14], who found that after crystallization, the films with larger grains have higher resistivities than the films with smaller grains.

The IZO6 sample with the lowest electrical resistivity was additionally annealed in Ar/H_2. The electrical resistivity decreased significantly from 0.45 Ωcm to 0.0069 mΩcm for IZO6 and IZO6-Ar/H_2. While the thickness, structure, microstructure, grain size and surface roughness of these two thin films were similar, the significant increase in conductivity upon post-annealing in Ar/H_2 is likely to occur in conjunction with defect concentration and mobility. The conduction electrons in IZO are supplied from native defects, i.e., oxygen vacancies, and from substitutions/interstitial zinc and indium ions [15]. Upon heating the IZO thin films in a hydrogen-containing atmosphere, the hydrogen can incorporate into the structure at the interstitial positions and this increases the electrical conductivity of the IZO [16,44]. An improved electrical conductivity upon post-annealing the thin films in a reducing atmosphere is in agreement with the literature [9,11,29]. The electrical resistivity values obtained in this study are comparable or lower than those obtained for thin films produced by chemical solution deposition with a similar nominal chemical composition [11,13,45]. The electrical resistivity of magnetron-sputtered thin films with a similar chemical composition is slightly lower [20].

3.3. Optical properties

The optical properties of the sample IZO6 were determined from the variable-angle spectroscopic ellipsometry (VASE). The experimental ellipsometric spectra [Ψ,Δ](λ) for the sample IZO6 are presented in Fig. 8 a and b, in which the solid lines represent the best-fit functions calculated from the optical model (see inset figures). An experiment performed with a replica sample resulted in a coincident spectrum (not shown). In order to achieve a satisfactory fit, it was necessary to involve a uniaxially anisotropic refractive-index dispersion for the film, where the ordinary component is the Tauc-Lorentz-Urbach (TLU) oscillator and the extraordinary

component is represented by a constant and purely real refractive index. An extremely good fit is observed for both Δ (cf. Fig. 8 a) and Ψ (cf. Fig. 8 b) throughout the whole measured range of λ, irrespective of the AOI, which is important for fitting the parameters related to the Lorentz oscillator representing the principal absorption in the far-UV region, and thus outside the experimental wavelength range. The best-fit parameters of the TLU oscillator and their confidence intervals are in Table 3 (please note that $\tilde{\varepsilon} = \tilde{n}^2$).

While the model curves fit the data very well, the TLU oscillator strength (A) and width (Γ) exhibit relatively large confidence intervals, which is a consequence of their mathematical coupling in the expression of the Lorentz oscillator, as well as the fact that this absorption is found outside the experimental wavelength window. The best-fit complex refractive-index dispersion for IZO6, calculated from the TLU parameters in Table 3 and is presented in Fig. 9a. The ordinary component exhibits absorption in the UV region of the spectrum (as inferred from k_{ord}), while its real part (n_{ord}) does not exhibit a large variation and is similar in magnitude to the extraordinary refractive index (n_{ex}). The extraordinary component is purely real and constant (fitted as $n_{ex} = 1.613 \pm 0.002$).

While the Tauc-Lorentz (TL) dispersion relies on a simplified picture of the energy gap, stipulating a parabolic density of states near E_g and no absorption at energies below the gap ($k = 0; E \leq E_g$), in the TLU dispersion, the exponential "Urbach tail" is introduced for the transitions involving the in-the-gap states [33]. For the principal absorption edge near the band-gap energies (E larger but not much larger than E_t), both dispersions predict an absorption-coefficient dependency of the form $(\alpha(E)n(E)E)^{1/2} \approx E$, valid for the description of indirect, allowed absorption edges encountered in amorphous semiconductors [46,47]. For a full description of the mathematical derivation and the properties for the two dispersions, please refer to the paper by Ferlauto et al. [33]. Thus, the fact that the TLU oscillator, representing an indirect gap, was found to best fit the ellipsometric spectra, is in line with the amorphous structure of IZO. The features of the TLU dispersion in relation to its parameters, can be inferred by inspecting the k-dispersion presented in Fig. 9a. There are two characteristic ranges of this function, from high to low energy. The Lorentz oscillator characterizes the principal electronic transition and is dominant at energies $\geq E_t$. The latter energy is identified with the optical gap that defines the high-energy onset of the in-the-gap absorption, marked by a discontinuity in the 1st derivative of the k-dispersion. The energy E_g denotes the ″pure″ Tauc gap, which was introduced by Jellison and Modine as the low-energy onset of the principal transition in the TL dispersion [48] and is detected as the extrapolation of the $[\alpha h\nu]^{1/2}$ vs. E plot at $\alpha = 0$, presented in Fig. 9b. In the TLU dispersion, the exponential Urbach tail overtakes the Lorentz oscillator at $E < E_t$, in which region the parameter E_u defines the decay energy related to the widening of the joint density of states, often related to the structural "disorder" or the presence of defects in the electronic structure [33,49,50]. In the case of IZO6, the fitted value of E_u is relatively large, compared to the values obtained for lightly In-doped ZnO magnetron-sputtered films with a high level of crystallinity [17].

From the imaginary refractive-index dispersion presented in Fig. 9a, it is straightforward to calculate the absorption coefficient as $\alpha = 4\pi k/\lambda$ [32], which according to the TLU model, results in the linear dependency of $[\alpha h\nu]^{1/2}$ vs. E just above E_t, as presented in Fig. 9b. The E_t of the studied IZO6 film is found to be closer to the gap energy of the nanocrystalline In_2O_3 (2.70 eV [51]) than that of ZnO ($\gtrsim 3$, 30 eV, depending on the phase type and the preparation route [50,52–54]), which is in line with the stoichiometric predominance of In over Zn in the structure of IZO. By relating this with the aforementioned findings [17,18] it can be concluded that the stoichiometric ratio In:Zn in IZO predominantly determines the band-gap energy. From the transmission spectrum of the IZO6 film at normal incidence, calculated from the ordinary dispersion [32] and plotted on the right-hand axis of Fig. 9b, it becomes evident that the highest transparency of the film (92.5%) is observed around the gap energy, corresponding to the wavelength $\lambda = 450$ nm, and is larger than 80% throughout the visible range. In this respect, it becomes clear that increasing the band-gap energy of IZO6 would result in higher transparency over a broader range of wavelengths.

The optical anisotropy observed from the ellipsometric spectra of IZO6 is a consequence of the applied optical model. In reality, the thin lamellae that separate the IZO layers should exhibit a different dispersion from IZO, which is evident from the higher electron density in these lamellae than with IZO, observed with SEM. The refractive-index dispersion of these lamellae, treated as a separate optical phase, could not be resolved from the SE data. Nevertheless, their overall effect on the light propagation in the film is detected as optical anisotropy of the film, treated as a single (homogeneous) optical phase. Therefore, the observed optical anisotropy is a consequence of the lamellar nano-scale structure and should not be confused with the birefringence assigned to individual optical phases. Since the extraordinary dispersion fitted from the ellipsometric spectra does not exhibit absorption ($k_{ex} = 0$), it can be deduced that the extraordinary light beam experiences only a phase shift due to the presence of lamellae. While this effect should be detectable only with ellipsometry as a light-phase sensitive measurement performed at an oblique angle of incidence with respect to the film's surface, it nevertheless deserves to be studied in more detail for films prepared by chemical solution deposition, as it could lead to optical-properties tailoring through a simple variation in the number of layers.

4. Conclusions

Indium-zinc-oxide (IZO) thin films with a Zn/(In + Zn) molar ratio of 0.36 on glass were prepared by spin-coating a solution of zinc

Table 3
Best-fit parameters of the TLU oscillator representing the ordinary component of the dielectric function for IZO6 (parameter notation according to Ref. [33]).

ε_∞	A/eV	E_0/eV	Γ/eV	E_g/eV	E_t/eV	E_u/eV
1.940	39.641	5.508	7.485	2.571	2.819	0.895
±0.232	±17.175	±0.714	±4.412	±0.070	±0.083	±0.137

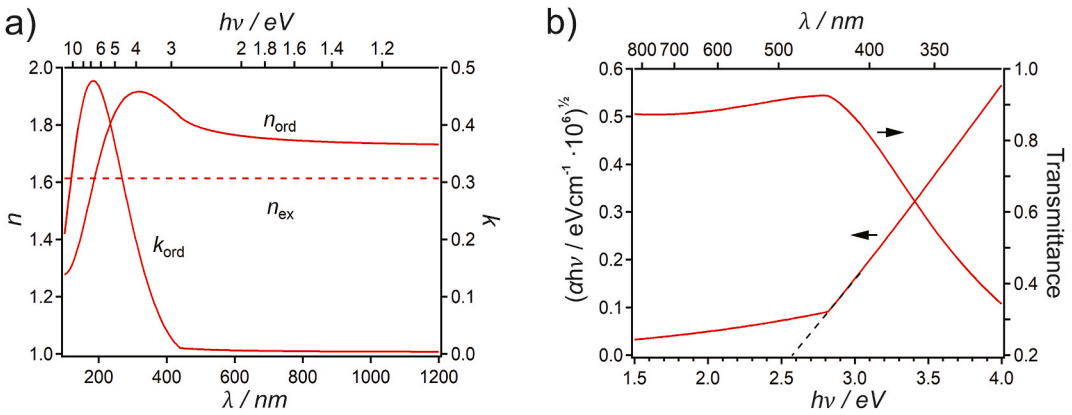

Fig. 9. a) Best-fit refractive-index dispersion for IZO6. The ordinary component of the uniaxially anisotropic dispersion described by the TLU oscillator (parameters in Table 3) while the extraordinary component is a constant *n*, indicated with the dashed line. b) The Tauc plot (left axis), calculated from the imaginary ordinary refractive index; and transmittance at normal incidence (right axis), calculated from the ordinary dispersion.

acetate hydrate and indium nitrate dissolved in ethylene glycol and ethanol. Based on a thermal analysis the coatings were dried at 200 and 350 °C and then annealed in air at 500, 600, and 700 °C. An XRD analysis showed that none of the thin films exhibited long-range ordering, regardless of annealing temperature. Upon increasing the annealing temperature, the grain size and the RMS surface roughness of the film increased, while simultaneously the thickness decreased. The 115-nm- thick films annealed at 600 °C exhibited a lamellar structure that vanished when heated to 700 °C. The electrical resistivity of the films depended on the annealing temperature. The lowest value, 0.45 Ωcm, was obtained for the IZO thin film annealed at 600 °C in air, which can be attributed to the organic-free composition, the amorphous nature of the film with 20-nm grains, and the homogeneous microstructure. After annealing this film in Ar/H_2, the electrical resistivity decreased by more than an order of magnitude to 0.0069 Ωcm, which can be ascribed to the increasing defect concentration and their mobility, rather than to the thickness, grain size, structural and microstructural properties of the thin films. The IZO film cured at 600 °C exhibited uniaxial optical anisotropy due to the lamellar nanostructure, in which the IZO layers are separated by ultra-thin lamellae with a higher electron density. The ordinary refractive index is successfully fitted as a Tauc-Lorentz-Urbach function, which is typical of an indirect absorption edge occurring in amorphous semiconductor materials. The principal absorption peak is found in the UV region, with an onset at about 2.8 eV, while the Tauc gap energy is about 2.6 eV. These values are similar to those observed for In_2O_3 and are much lower than the gap energy of ZnO.

The described low-cost, vacuum-free spin coating followed by post-deposition curing makes it possible to tune the microstructure of the IZO thin films and thus their amorphous nature, electrical conductivity, and optical properties. This process is promising for the cost-effective fabrication of IZO thin films for transparent electronics.

Funding

This research was funded by the Slovenian Research Agency (grant numbers P2-0105, P2-0082 and L2-4469).

Author contribution statement

Izabela Stojanoska, Miha Okorn, Brigita Kmet: Performed the experiments; Analyzed and interpreted the data. Hana Uršič;, Vera Gradišnik, Duško Čakara, Janez Kovač;: Conceived and designed the experiments; Performed the experiments; Analyzed and interpret the data; Contributed reagents, materials, analysis tools or data; Wrote the paper. Danjela Kuscer: Conceived and designed the experiments; Analyzed and interpreted the data; Contributed reagents, materials, analysis tools or data; Wrote the paper.

Data availability statement

Data will be made available on request.

Declaration of competing interest

The authors declare that they have no known competing financial interests or personal relationships that could have appeared to influence the work reported in this paper.

5 Acknowledgements

We thank Dr. Urška Trstenjak for performing the XRD analyses, Jena Cilenšek for performing the thermal analyses, Sabi William

Konsago for help with the FTIR, Val Fišinger and Alaka Panda for help with the AFM and Prof. Tadej Rojac for help with the R_s measurements.

Appendix A. Supplementary data

Supplementary data to this article can be found online at https://doi.org/10.1016/j.heliyon.2023.e19744.

References

[1] S. Bae, S.J. Kim, D. Shin, J.-H. Ahn, B.H. Hong, Towards industrial applications of graphene electrodes, Phys. Scripta 2012 (2012), 014024, https://doi.org/10.1088/0031-8949/2012/T146/014024.

[2] W. Cui, F. Chen, Y. Li, X. Su, B. Sun, Status and perspectives of transparent conductive oxide films for silicon heterojunction solar cells, Mater, Today Nano 22 (2023), 100329, https://doi.org/10.1016/j.mtnano.2023.100329.

[3] B.K. Yap, Z. Zhang, G.S.H. Thien, K.-Y. Chan, C.Y. Tan, Recent advances of In_2O_3-based thin-film transistors: a review, Appl. Surf. Sci. Adv. 16 (2023), 100423, https://doi.org/10.1016/j.apsadv.2023.100423.

[4] N.M. Khusayfan, M.M. El-Nahass, Study of structure and electro-optical characteristics of indium tin oxide thin films, Adv. Condens. Matter Phys. 2013 (2013), e408182, https://doi.org/10.1155/2013/408182.

[5] B. Janarthanan, C. Thirunavukkarasu, S. Maruthamuthu, M.A. Manthrammel, Mohd Shkir, S. AlFaify, M. Selvakumar, V.R.M. Reddy, C. Park, Basic deposition methods of thin films, J. Mol. Struct. 1241 (2021), 130606, https://doi.org/10.1016/j.molstruc.2021.130606.

[6] K. Nomura, H. Ohta, A. Takagi, T. Kamiya, M. Hirano, H. Hosono, Room-temperature fabrication of transparent flexible thin-film transistors using amorphous oxide semiconductors, Nature 432 (2004) 488–492, https://doi.org/10.1038/nature03090.

[7] S.-Y. Lee, B.-O. Park, Electrical and optical properties of In_2O_3–ZnO thin films prepared by sol–gel method, Thin Solid Films 484 (2005) 184–187, https://doi.org/10.1016/j.tsf.2005.03.007.

[8] D.C. Paine, B. Yaglioglu, Z. Beiley, S. Lee, Amorphous IZO-based transparent thin film transistors, Thin Solid Films 516 (2008) 5894–5898, https://doi.org/10.1016/j.tsf.2007.10.081.

[9] M.P. Taylor, D.W. Readey, M.F.A.M. van Hest, C.W. Teplin, J.L. Alleman, M.S. Dabney, L.M. Gedvilas, B.M. Keyes, B. To, J.D. Perkins, D.S. Ginley, The remarkable thermal stability of amorphous in-Zn-O transparent conductors, Adv. Funct. Mater. 18 (2008) 3169–3178, https://doi.org/10.1002/adfm.200700604.

[10] M. Morales-Masis, S. Martin De Nicolas, J. Holovsky, S. De Wolf, C. Ballif, Low-temperature high-mobility amorphous IZO for silicon heterojunction solar cells, IEEE J. Photovoltaics 5 (2015) 1340–1347, https://doi.org/10.1109/JPHOTOV.2015.2450993.

[11] S. Ullah, R. Branquinho, A. Santa, F. De Matteis, R. Martins, I. Davoli, G. Gonçalves, E. Fortunato, Boosting highly transparent and conducting indium zinc oxide thin films through solution combustion synthesis: influence of rapid thermal annealing, Semicond. Sci. Technol. 33 (2018), 105004, https://doi.org/10.1088/1361-6641/aad5cc.

[12] D.-C. Tsai, Z.-C. Chang, B.-H. Kuo, Y.-H. Wang, E.-C. Chen, F.-S. Shieu, Thickness dependence of the structural, electrical, and optical properties of amorphous indium zinc oxide thin films, J. Alloys Compd. 743 (2018) 603–609, https://doi.org/10.1016/j.jallcom.2017.12.062.

[13] I. Choudhary, Deepak, Investigation of time-dependent stability and surface defects in sol–gel derived IGZO and IZO thin films, J. Sol. Gel Sci. Technol. 100 (2021) 132–146, https://doi.org/10.1007/s10971-021-05615-w.

[14] A. Steigert, D. Kojda, J. Ibaceta-Jaña, D. Abou-Ras, R. Gunder, N. Alktash, K. Habicht, M.R. Wagner, R. Klenk, S. Raoux, B. Szyszka, I. Lauermann, R. Muydinov, Water-assisted crystallization of amorphous indium zinc oxide films, Mater. Today Commun. 31 (2022), 103213, https://doi.org/10.1016/j.mtcomm.2022.103213.

[15] H. Peng, J.-H. Song, E.M. Hopper, Q. Zhu, T.O. Mason, A.J. Freeman, Possible *n*– type carrier sources in In_2O_3 $(ZnO)_k$, Chem. Mater. 24 (2012) 106–114, https://doi.org/10.1021/cm202020g.

[16] C.G. Van de Walle, Hydrogen as a cause of doping in zinc oxide, Phys. Rev. Lett. 85 (2000) 1012–1015, https://doi.org/10.1103/PhysRevLett.85.1012.

[17] Y. Cao, L. Miao, S. Tanemura, M. Tanemura, Y. Kuno, Y. Hayashi, Y. Mori, Optical properties of indium-doped ZnO films, Jpn. J. Appl. Phys. 45 (2006) 1623–1628, https://doi.org/10.1143/JJAP.45.1623.

[18] N. Vasile, S. Iftimie, T. Acsente, C. Locovei, A.I. Călugăr, A. Radu, L. Ion, V.-A. Antohe, D. Manica, O. Toma, G. Dinescu, Ş. Antohe, Physical properties of indium zinc oxide and aluminium zinc oxide thin films deposited by radio-frequency magnetron sputtering, Mater. Res. Express 6 (2020), 126447, https://doi.org/10.1088/2053-1591/ab688d.

[19] T. Minami, T. Kakumu, Y. Takeda, S. Takata, Highly transparent and conductive ZnO-In_2O_3 thin films prepared by d.c. magnetron sputtering, Thin Solid Films 290–291 (1996) 1–5, https://doi.org/10.1016/S0040-6090(96)09094-3.

[20] N. Naghavi, L. Dupont, C. Marcel, C. Maugy, B. Laık, A. Rougier, C. Guéry, J.M. Tarascon, Systematic study and performance optimization of transparent conducting indium–zinc oxides thin films, Electrochim. Acta 46 (2001) 2007–2013, https://doi.org/10.1016/S0013-4686(01)00417-0.

[21] M.F. Malek, M.H. Mamat, M.Z. Musa, Z. Khusaimi, M.Z. Sahdan, A.B. Suriani, A. Ishak, I. Saurdi, S.A. Rahman, M. Rusop, Thermal annealing-induced formation of ZnO nanoparticles: minimum strain and stress ameliorate preferred c-axis orientation and crystal-growth properties, J. Alloys Compd. 610 (2014) 575–588, https://doi.org/10.1016/j.jallcom.2014.05.036.

[22] M.A. Shafi, A. Bouich, K. Fradi, J.M. Guaita, L. Khan, B. Mari, Effect of deposition cycles on the properties of ZnO thin films deposited by spin coating method for CZTS-based solar cells, Optik 258 (2022), 168854, https://doi.org/10.1016/j.ijleo.2022.168854.

[23] R.M. Pasquarelli, D.S. Ginley, R. O'Hayre, Solution processing of transparent conductors: from flask to film, Chem. Soc. Rev. 40 (2011) 5406, https://doi.org/10.1039/c1cs15065k.

[24] R.W. Schwartz, T. Schneller, R. Waser, Chemical solution deposition of electronic oxide films, Compt. Rendus Chem. 7 (2004) 433–461, https://doi.org/10.1016/j.crci.2004.01.007.

[25] X. Li, Q. Li, E. Xin, J. Zhang, Sol–gel processed indium zinc oxide thin film and transparent thin-film transistors, J. Sol. Gel Sci. Technol. 65 (2013) 130–134, https://doi.org/10.1007/s10971-012-2916-2.

[26] J. Tellier, B. Malic, D. Kuscer, G. Trefalt, M. Kosec, Ink-jet printing of In_2O_3/ZnO two-dimensional structures from solution, J. Am. Ceram. Soc. 94 (2011) 2834–2840, https://doi.org/10.1111/j.1551-2916.2011.04425.x.

[27] G.H. Kim, H.S. Kim, H.S. Shin, B.D. Ahn, K.H. Kim, H.J. Kim, Inkjet-printed InGaZnO thin film transistor, Thin Solid Films 517 (2009) 4007–4010, https://doi.org/10.1016/j.tsf.2009.01.151.

[28] M. Caglar, S. Ruzgar, Influence of the deposition temperature on the physical properties of high electron mobility ZnO films by sol–gel process, J. Alloys Compd. 644 (2015) 101–105, https://doi.org/10.1016/j.jallcom.2015.04.167.

[29] N. Beji, M. Souli, S. Azzaza, S. Alleg, N. Kamoun Turki, Study on the zinc doping and annealing effects of sprayed In_2O_3 thin films, J. Mater. Sci. Mater. Electron. 27 (2016) 4849–4860, https://doi.org/10.1007/s10854-016-4367-y.

[30] J.F. Moulder, W.F. Stickle, P.E. Sobol, K.D. Bomben, Handbook of X-Ray Photoelectron Spectroscopy, Physical Electronics Inc., Eden Prairie, Minnesota, USA, 1995.

[31] D.K. Schroder. Semiconductor Material and Device Characterization, 3th ed., John Wiley & Sons, Inc, Hoboken, NY, USA, 2005.

[32] H. Fujiwara, Spectroscopic Ellipsometry: Principles and Applications, John Wiley & Sons Ltd., Chichester, UK, 2007.
[33] A.S. Ferlauto, G.M. Ferreira, J.M. Pearce, C.R. Wronski, R.W. Collins, X. Deng, G. Ganguly, Analytical model for the optical functions of amorphous semiconductors from the near-infrared to ultraviolet: applications in thin film photovoltaics, J. Appl. Phys. 92 (2002) 2424–2436, https://doi.org/10.1063/1.1497462.
[34] J. Wang, Y. Qi, Z. Zhi, J. Guo, M. Li, Y. Zhang, A self-assembly mechanism for sol–gel derived ZnO thin films, Smart Mater. Struct. 16 (2007) 2673, https://doi.org/10.1088/0964-1726/16/6/072.
[35] J. Leppäniemi, O.-H. Huttunen, H. Majumdar, A. Alastalo, Flexography-Printed In_2O_3 semiconductor layers for high-mobility thin-film transistors on flexible plastic substrate, Adv. Mater. 27 (2015) 7168–7175, https://doi.org/10.1002/adma.201502569.
[36] I. Winer, G.E. Shter, M. Mann-Lahav, G.S. Grader, Effect of solvents and stabilizers on sol–gel deposition of Ga-doped zinc oxide TCO films, J. Mater. Res. 26 (2011) 1309–1315, https://doi.org/10.1557/jmr.2011.69.
[37] J. Gan, X. Lu, J. Wu, S. Xie, T. Zhai, M. Yu, Z. Zhang, Y. Mao, S.C.I. Wang, Y. Shen, Y. Tong, Oxygen vacancies promoting photoelectrochemical performance of In_2O_3 nanocubes, Sci. Rep. 3 (2013) 1021, https://doi.org/10.1038/srep01021.
[38] G. Shao, X. Wu, Y. Kong, S. Cui, X. Shen, C. Jiao, J. Jiao, Thermal shock behavior and infrared radiation property of integrative insulations consisting of $MoSi_2$/borosilicate glass coating and fibrous ZrO_2 ceramic substrate, Surf. Coat. Technol. 270 (2015) 154–163, https://doi.org/10.1016/j.surfcoat.2015.03.008.
[39] G. Socrates. Infrared Characteristic Group Frequencies Tables and Charts, 2nd ed., John Wiley & Sons Ltd, Chichester, UK, 1994.
[40] T. Moriga, D.D. Edwards, T.O. Mason, G.B. Palmer, K.R. Poeppelmeier, J.L. Schindler, C.R. Kannewurf, I. Nakabayashi, Phase relationships and physical properties of homologous compounds in the zinc oxide-indium oxide system, J. Am. Ceram. Soc. 81 (2005) 1310–1316, https://doi.org/10.1111/j.1151-2916.1998.tb02483.x.
[41] D.-H. Lee, Y.-J. Chang, G.S. Herman, C.-H. Chang, A general route to printable high-mobility transparent amorphous oxide semiconductors, Adv. Mater. 19 (2007) 843–847, https://doi.org/10.1002/adma.200600961.
[42] L. Xu, W. Kuang, F. Xian, X. Wang, Tailoring the optical properties of ZnO thin films with a double-layer structure: the role of annealing temperature, Surface. Interfac. 21 (2020), 100658, https://doi.org/10.1016/j.surfin.2020.100658.
[43] I. Stojanoska, B. Kmet, H. Uršič, D. Kuscer, Gallium-modified zinc oxide thin films prepared by chemical solution deposition, Crystals 13 (2023) 1030, https://doi.org/10.3390/cryst13071030.
[44] S.F.J. Cox, E.A. Davis, S.P. Cottrell, P.J.C. King, J.S. Lord, J.M. Gil, H.V. Alberto, R.C. Vilão, J. Piroto Duarte, N. Ayres de Campos, A. Weidinger, R.L. Lichti, S.J. C. Irvine, Experimental confirmation of the predicted shallow donor hydrogen state in zinc oxide, Phys. Rev. Lett. 86 (2001) 2601–2604, https://doi.org/10.1103/PhysRevLett.86.2601.
[45] J.-H. Lee, S.-Y. Lee, B.-O. Park, Fabrication and characteristics of transparent conducting In_2O_3–ZnO thin films by ultrasonic spray pyrolysis, Mater. Sci. Eng. B. 127 (2006) 267–271, https://doi.org/10.1016/j.mseb.2005.10.008.
[46] N.F. Mott, S.N.F. Mott, E.A. Davis, Electronic Processes in Non-crystalline Materials, 2nd ed., OUP Oxford, NY, USA, 2012.
[47] M. Bass, in: Optical Society of America, Handbook of Optics, 2nd ed., McGraw-Hill Inc., NY, USA, 1995.
[48] M. Jellison, Parameterization of the optical functions of amorphous materials in the interband region, Appl. Phys. Lett. n.d. (1996) 371–373, https://doi.org/10.1063/1.118064.
[49] D.V. Tsu, T. Schuelke, J. Slagter, Optical measure of disorder: why Urbach analysis works for amorphous silicon but fails for amorphous carbon, Diam. Relat. Mater. 110 (2020), 108137, https://doi.org/10.1016/j.diamond.2020.108137.
[50] R. Vettumperumal, S. Kalyanaraman, B. Santoshkumar, R. Thangavel, Estimation of electron–phonon coupling and Urbach energy in group-I elements doped ZnO nanoparticles and thin films by sol–gel method, Mater. Res. Bull. 77 (2016) 101–110, https://doi.org/10.1016/j.materresbull.2016.01.015.
[51] E.A. Forsh, A.M. Abakumov, V.B. Zaytsev, E.A. Konstantinova, P.A. Forsh, M.N. Rumyantseva, A.M. Gaskov, P.K. Kashkarov, Optical and photoelectrical properties of nanocrystalline indium oxide with small grains, Thin Solid Films 595 (2015) 25–31, https://doi.org/10.1016/j.tsf.2015.10.053.
[52] K.-F. Lin, H.-M. Cheng, H.-C. Hsu, L.-J. Lin, W.-F. Hsieh, Band gap variation of size-controlled ZnO quantum dots synthesized by sol–gel method, Chem. Phys. Lett. 409 (2005) 208–211, https://doi.org/10.1016/j.cplett.2005.05.027.
[53] S.A. Studenikin, N. Golego, M. Cocivera, Fabrication of green and orange photoluminescent, undoped ZnO films using spray pyrolysis, J. Appl. Phys. 84 (1998) 2287–2294, https://doi.org/10.1063/1.368295.
[54] M.R. Islam, M. Rahman, S.F.U. Farhad, J. Podder, Structural, optical and photocatalysis properties of sol–gel deposited Al-doped ZnO thin films, Surface. Interfac. 16 (2019) 120–126, https://doi.org/10.1016/j.surfin.2019.05.007.